catalysts

Supporting Information

Enhanced alkaline hydrogen evolution on $Gd_{1.0}$-Nd_x (x = 0.5, 1.0, 3.0, and 6.0%)-doped TiO_2 bimetallic electrocatalysts

S1. Characterization of Gd_x/TiO_2, Nd_x/TiO_2, and $Gd_{1.0}/Nd_x/TiO_2$ NPs

The formation of Gd_x/TiO_2, Nd_x/TiO_2, and $Gd_{0.5}/Nd_{0.5}/TiO_2$ NPs was characterized by FT-IR and simultaneous TGA-DTA analysis, **Figures S1** and **S2)**. The solvolysis of titanium(IV) *tert*-butoxide in presence of gadolinium(III) or neodymium(III) salts in dimethyl sulfoxide (DMSO) as a solvent (and as a reactant) leads to the spontaneous formation of Gd^{3+}·$Ti(OH)_4$ or Nd^{3+}·$Ti(OH)_4$ monomers. As the temperature increases, these hydroxide monomers were then reacted with dimethyl sulfoxonium cation [1], which resulted from the decomposition of DMSO molecules grafted on the surfaces of Gd^{3+} or Nd^{3+}-doped TiO_2 NPs as initiators/catalysts.

The formation of $Ti(OH)_4$ as an intermediate on the surface of Gd^{3+} or Nd^{3+}-doped TiO_2 NPs slows down the growth of these NPs and prevents their agglomeration at high temperature [2]. Moreover, the presence of $Ti(OH)_4$ on the surface of these NPs acts as a nucleation site for the growth of Gd^{3+} or Nd^{3+}-doped TiO_2 NPs via inorganic polymerization reactions, which are also catalyzed by the high reactivity of the surfaces of Gd^{3+} or Nd^{3+}-doped TiO_2 NPs.

The FT-IR spectra of Gd^{3+}-doped TiO_2 NPs before and after the calcination process are displayed in **Figure S1**. The IR spectrum of the synthesized precursor Gd^{3+}.nBuO [3] shows a deformation vibration band of water at 1622 cm^{-1}, indicating its hydration nature. The spectrum also reveals the presence of butoxy groups (regions of 2800–3000 cm^{-1} and 1000–1250 cm^{-1}).

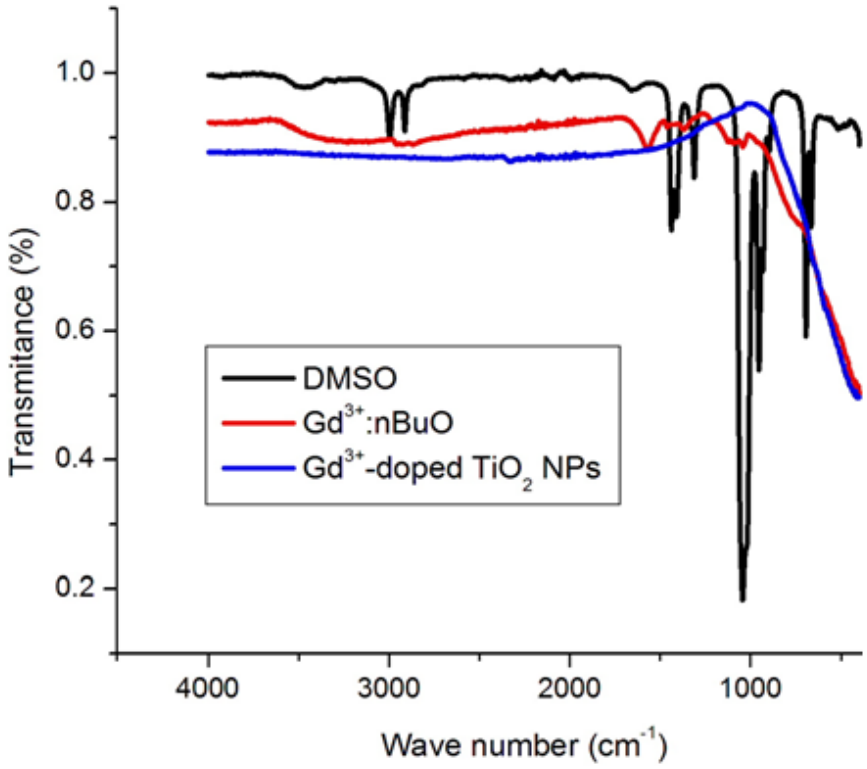

Figure S1. FT-IR spectra of DMSO, Gd^{3+}.nBuO, and Gd/TiO_2 NPs before (red) and after (blue) annealing process.

It also shows additional vibration bands at 1461 and 1377 cm^{-1}, which belong to methylene and methyl bending vibration bands [4,5]. The vibration band at 1438 cm^{-1} corresponds to the asymmetric bending (δ_{as}) of methyl groups in the DMSO molecule. The weak vibration bands around 1075 and 900 cm^{-1} can be assigned respectively to symmetric and asymmetric S–O stretching {ν_s(SO) and ν_{as}(SO)} vibrations of the bound DMSO molecules. Compared to pure DMSO, the spectrum of TiO_2 before annealing exhibits two additional peaks centered at 1584 and 3383 cm^{-1} due to δ_{H2O} bending and vibration of OH hydroxyl groups, respectively [6]. The peaks were not detected in the TiO_2 spectrum measured after the annealing process, which means that all organic compounds were removed from the samples by the calcination at 400 °C.

The thermal decomposition behavior of Gd^{3+}-doped TiO_2 NPs before and after the calcination process was examined by simultaneous thermogravimetric (TG) and differential thermal (DT) analysis between room temperature and 1000°C. **Figure S2** displays the DTA/TGA curves of Gd^{3+} and Nd^{3+}-doped TiO_2 nanoparticles before and after calcination process, respectively. According to **Figure S2(a)**, before calcination, the sample experienced four main degradation processes through the TGA test. The first step, occurred at about 110°C, was endothermic and could be due to the evaporation of a small amount of water molecules adsorbed on the TiO_2 surface as well as the volatilization of the remnant of organic solvents. The second process between 200 and 300°C was highly exothermic and could be attributed to the carbonization or the combustion of organic compounds. i.e. the loss of carbon, hydrogen, and oxygen. The third weight loss between 480 and 550 °C, accompanied by an exothermic peak, could be most likely ascribed to the further combustion of organic moieties [7,8] and crystallization of TiO_2 [9]. In the fourth step, small, but unexpected mass gain was observed, while slow mass loss took place at an almost constant rate. This result is in good agreement with the FT-IR measurement (result not shown), which confirms the presence of hydroxyl groups on the TiO_2 surface [10]. In contrast, no TGA weight loss or DTA peaks were detected in the TGA/DTA curves of Gd^{3+}-doped TiO_2 NPs recorded after calcination, **Figure S2(b)**. This indicates that the prepared Gd^{3+}-doped TiO_2NPs was highly thermally stable.

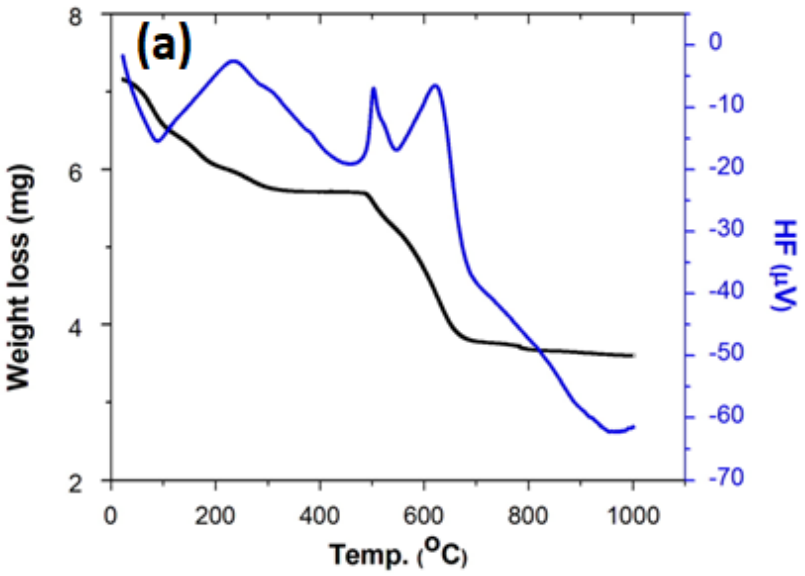

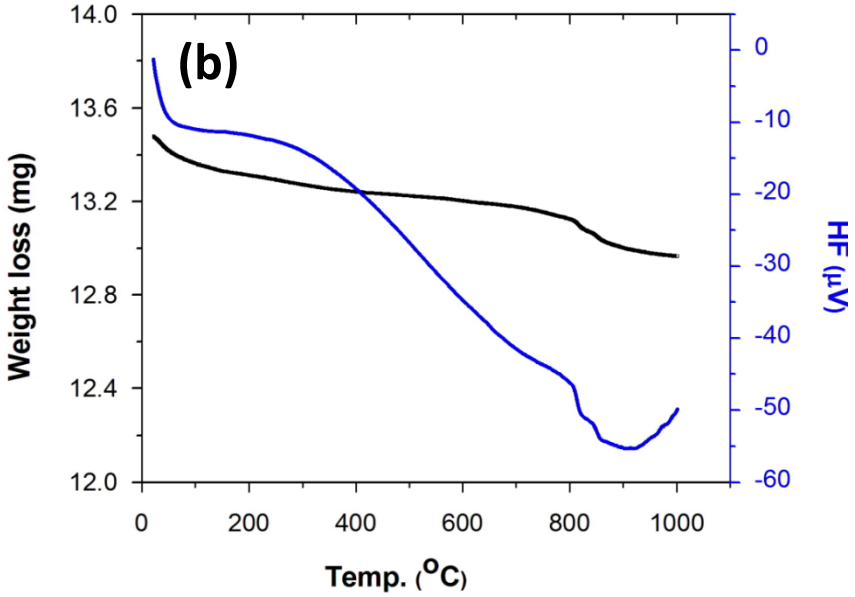

Figure S2. TGA-DTA curves of Gd_x/TiO_2 NPs recorded from room temperature to 1000°C before (a) and after (b) calcination.

S2. Preparation of the GC-loaded catalyst working electrode

A glassy carbon (GC) rod was polished using 0.3 and 0.05 microns size alumina powder until it had a mirror-like finish. Finally, it was dried in ambient after being ultrasonically cleaned for at least 20 min with double-distilled water (Milli-Q). The GC electrode was then loaded with the active material, producing GC-loaded catalyst working electrode. In this setup, an aqueous solution containing 0.5 wt.% Nafion was used to homogeneously disperse the catalyst powder in order to produce an ink. The catalyst ink was then obtained and drop-casted (20 μL, 1.0 mg/mL) over the freshly polished GC electrode. The catalyst had a loading density of about 0.28 mg cm^{-2}.

S3. Electrochemical characterizations

In an aqueous (deaerated) solution of KOH (1.0M), all electrochemical characterizations were carried out at room temperature. In each case, the WE's potential was measured against a Hg/HgO reference electrode and then converted to the scale of the reversible hydrogen electrode (RHE) using the formula $E_{RHE} = E_{Hg/HgO} + 0.059\ pH + 0.165$. The reproducibility of the electrochemical measurements was verified by performing each run at least three times, during which statistically significant results were collected. Each reported value's arithmetic mean and standard deviation were computed.

Linear sweep voltammetry (LSV) was used to evaluate the electrocatalytic activity of the designed catalysts for the HER. In order to run an LSV experiment, the working electrode was cathodically scanned from the corrosion potential (E_{corr}) to a cathodic potential of -1.0 V *vs.* SCE at a scan rate of 5.0 mV s^{-1}.

Using continuous cathodic potential cycling, the best catalyst described here, $Gd_{1.0}$-$Nd_{6.0}$-TiO_2, was evaluated for its long-term stability and durability. A complete cycle was formed by linearly sweeping the potential at a scan rate of 50 mV s^{-1} from the starting potential (E_{corr}) to the cathodic direction until it reached a cathodic potential of -1.0 V *vs.* RHE. Without taking the electrode out of the test solution, without time delay, the cycling process was repeated 10,000 times.

S4. HER's Faradaic efficiency measurements

The quantity of H_2 released (expressed in µmol) during a controlled galvanostatic electrolysis (CGE) was collected using gas chromatography (GC) to calculate the HER Faradaic efficiency values of the investigated catalysts. Measurements were performed in a custom-made airtight electrolysis cell. The H_2 gas evolved during the performed CGE was quantified by a GC conducted on an Agilent 7890A gas chromatograph with a pneumatically controlled automatic gas sampling valve. The electrolysis cell was connected to the GC device via bespoke airtight glass-to-metal adapters and copper tubing with an internal diameter of 1/8 in. The temperature of the furnace was set at 45 °C and the carrier gas was Ar, with a flow rate of about 3 mL min^{-1}.

The WE was subjected to a cathodic current density of -10 mA cm^{-2} for 1.0 h in 1.0 M KOH at room temperature. The volume of H_2 gas measured by GC is symbolized here as V_m, Eq. (S1).

$$V_m = \text{mol gas (GC)} \quad \text{(S1)}$$

The volume of H_2 theoretically estimated during the performed CGE run from the charge passed (assuming 100% Faradaic efficiency) through the working electrode (WE) is designated here as V_c, and calculated based on Eq. (S2) [11].

$$V_c = Q(\text{CGE}) / nF \quad \text{(S2)}$$

where F is the Faraday's constant (F = 96485 C) and Q(CGE) is the charge passed through the *WE* during the controlled process of galvanostatic electrolysis (CPE). The factor n represents the number of electrons transferred during the HER ($2H^+ + 2e^- = H_2$, n = 2). The value of *FE* is then calculated *via* dividing V_m by V_c. Finally, the tested electrocatalyst's *FE*% value is calculated *via* multiplying the quotient of the ratio (V_m/V_c) by 100, Eq. (S3) [11]:

$$\text{Faradaic efficiency (\%)} = [F \times n \times \text{mol gas (GC)} \times 100] / Q(\text{CGE}) \quad \text{(S3)}$$

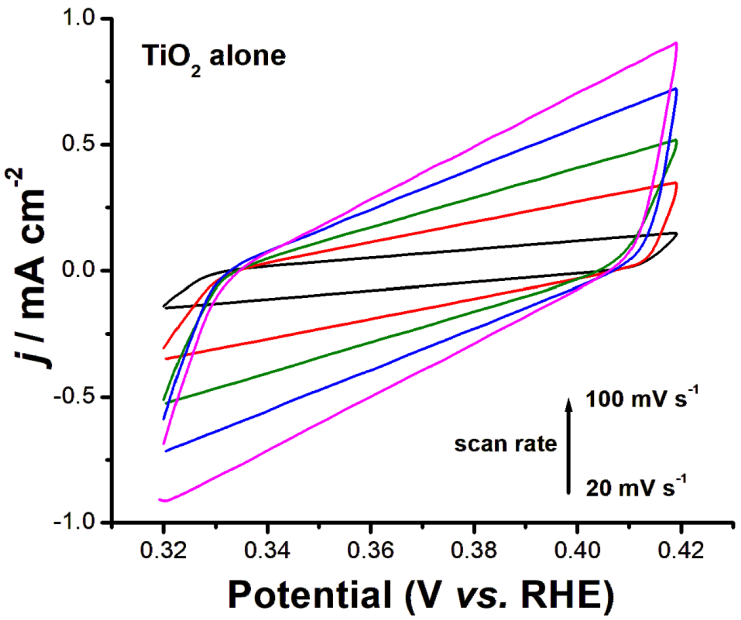

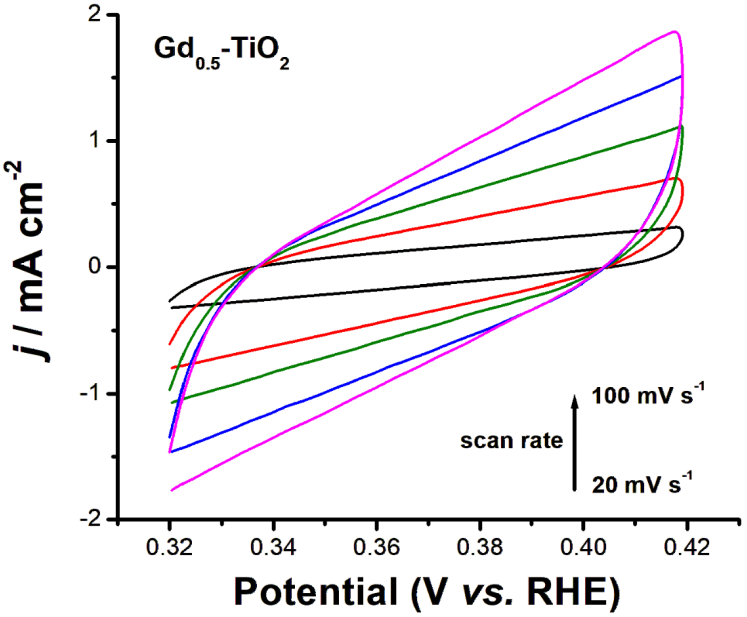
Gd0.5-TiO2
j / mA cm-2
Potential (V vs. RHE)
scan rate
100 mV s-1
20 mV s-1

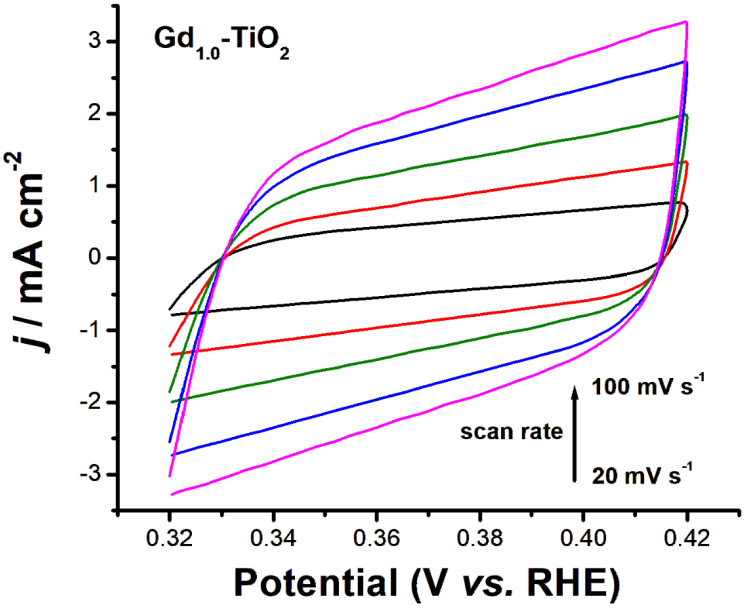
Gd1.0-TiO2
j / mA cm-2
Potential (V vs. RHE)
scan rate
100 mV s-1
20 mV s-1

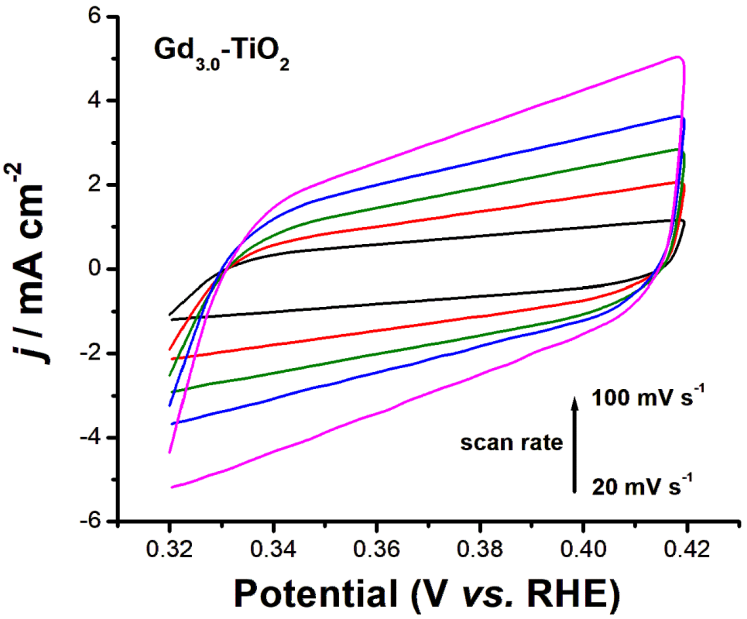
Gd3.0-TiO2
j / mA cm-2
Potential (V vs. RHE)
scan rate
100 mV s-1
20 mV s-1

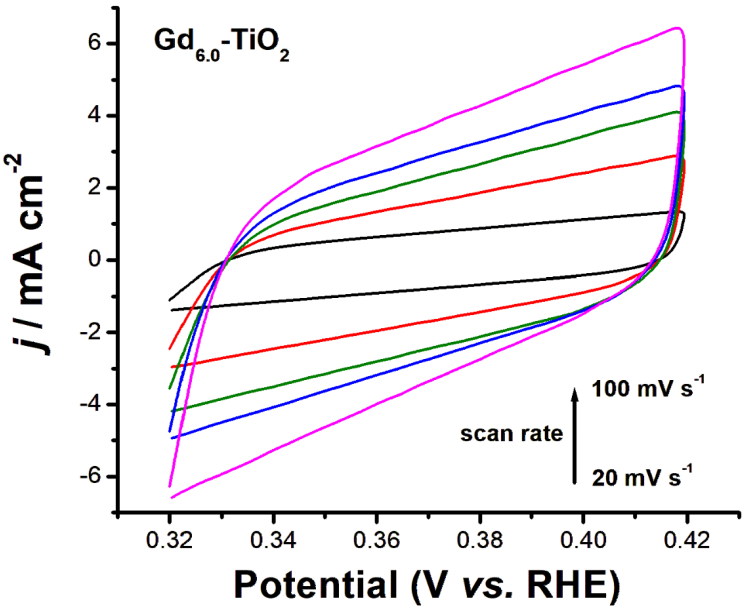
Gd6.0-TiO2
j / mA cm-2
Potential (V vs. RHE)
scan rate
100 mV s-1
20 mV s-1

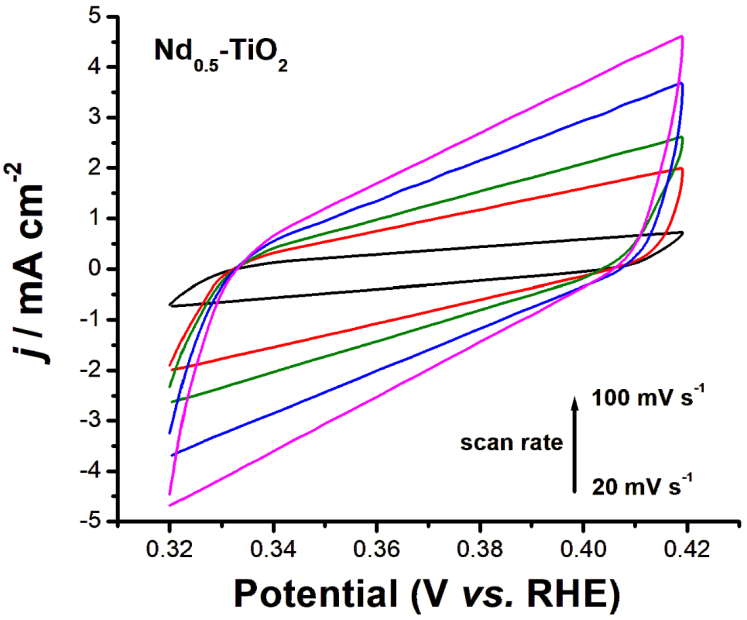
Nd0.5-TiO2
j / mA cm-2
Potential (V vs. RHE)
scan rate
100 mV s-1
20 mV s-1

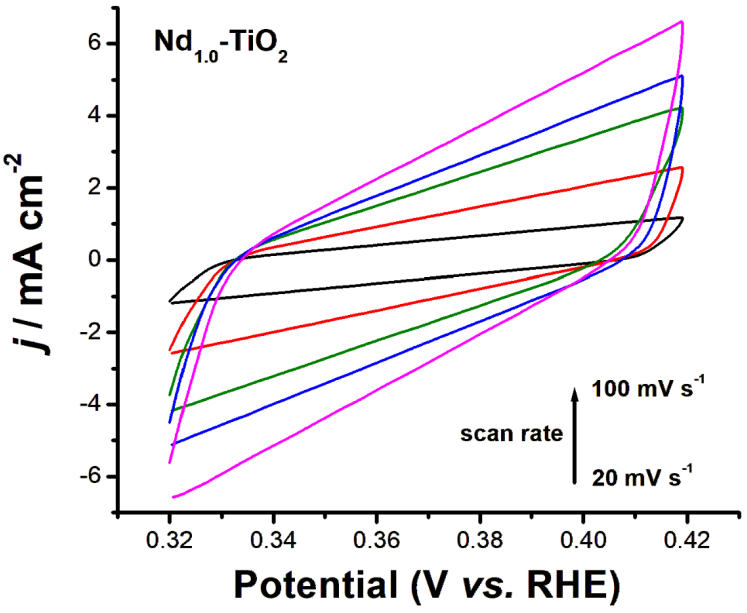
Nd1.0-TiO2
j / mA cm-2
Potential (V vs. RHE)
scan rate
100 mV s-1
20 mV s-1

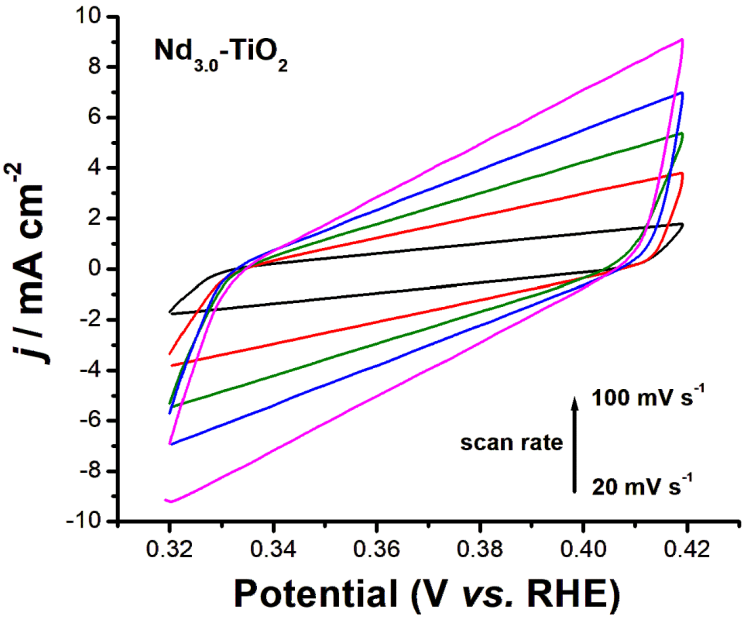
Nd3.0-TiO2
j / mA cm-2
Potential (V vs. RHE)
scan rate
100 mV s-1
20 mV s-1

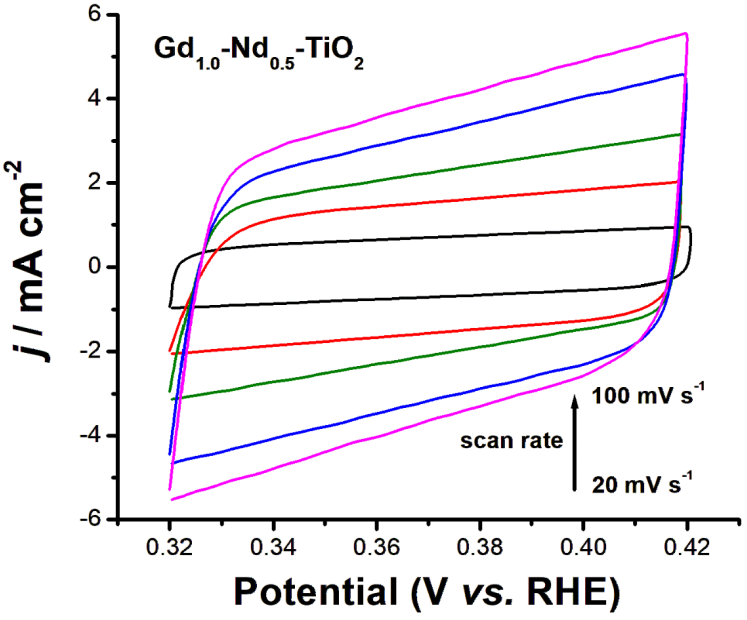
Gd1.0-Nd0.5-TiO2
j / mA cm-2
Potential (V vs. RHE)
scan rate
100 mV s-1
20 mV s-1

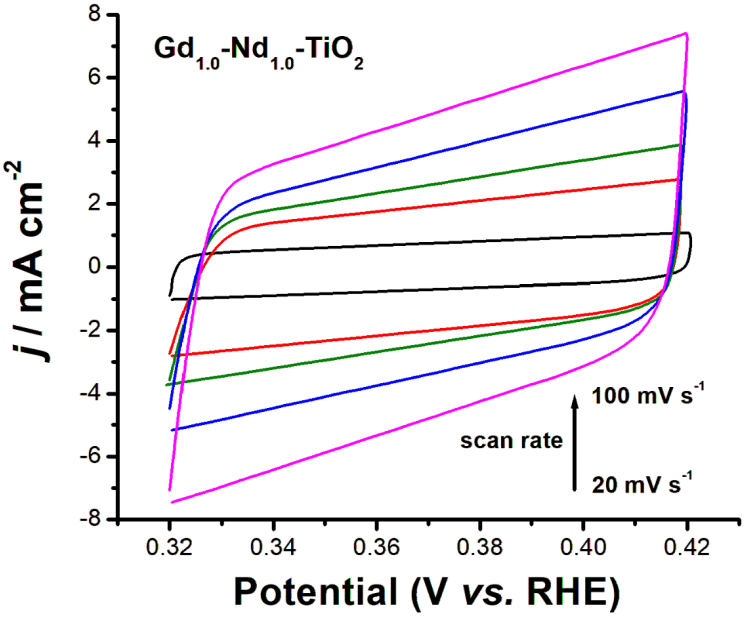
Gd1.0-Nd1.0-TiO2
j / mA cm-2
Potential (V vs. RHE)
scan rate
100 mV s-1
20 mV s-1

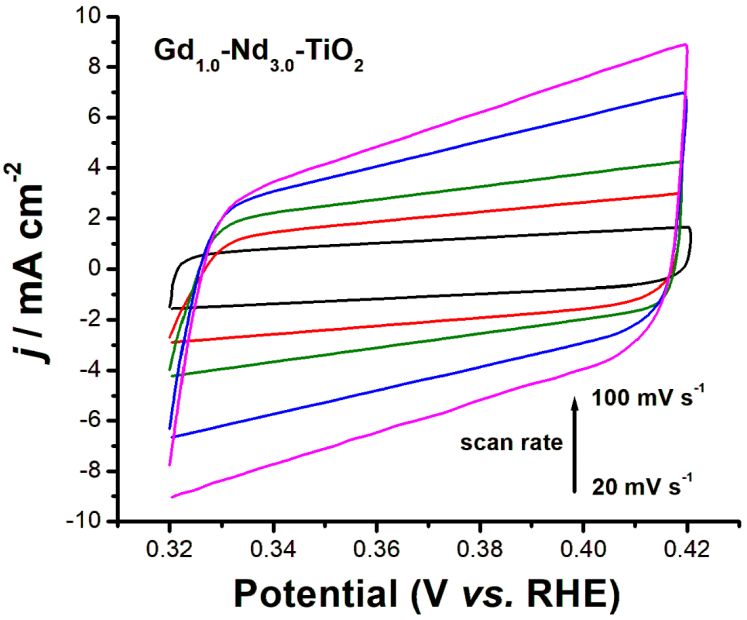
Gd1.0-Nd3.0-TiO2
j / mA cm-2
Potential (V vs. RHE)
scan rate
100 mV s-1
20 mV s-1

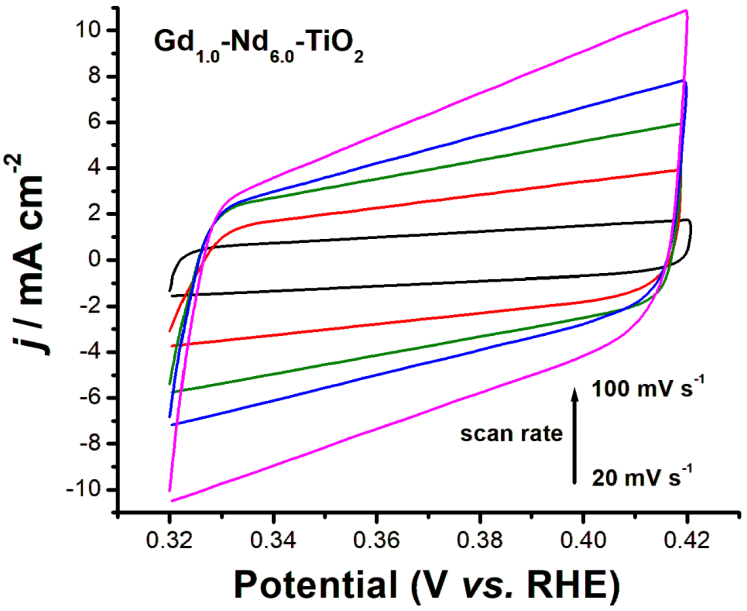

Figure S1. Cyclic voltammograms recorded for studied catalysts at various potential scan rates (20-100 mV s^{-1}) measured in a non-Faradaic region of the voltammograms. Measurements were conducted in deaerated KOH solution (1.0 M) at room temperature.

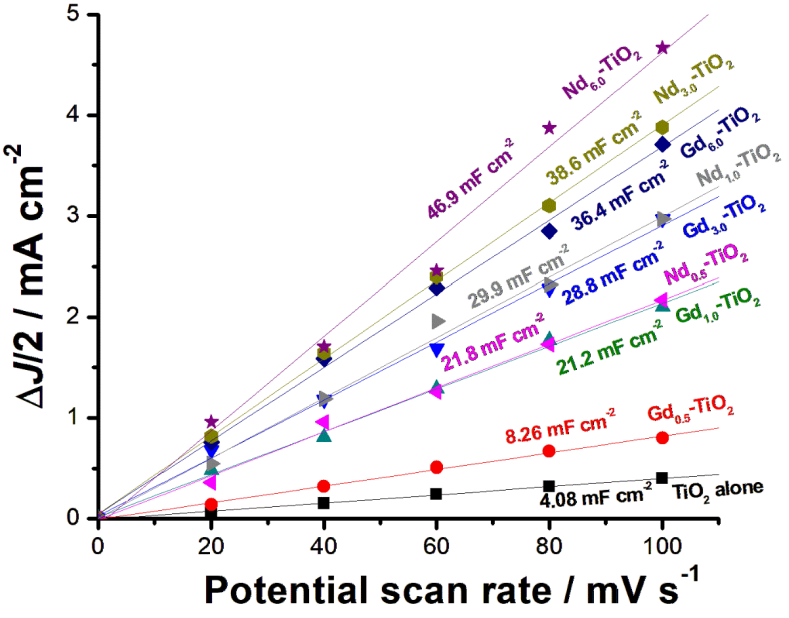

Figure S2. Double-layer capacitance measurements for determining the electrochemically-active surface area of Gd_x/TiO_2 and Nd_x/TiO_2 (x = 0.5, 1.0, 3.0, and 6.0 %) catalysts.

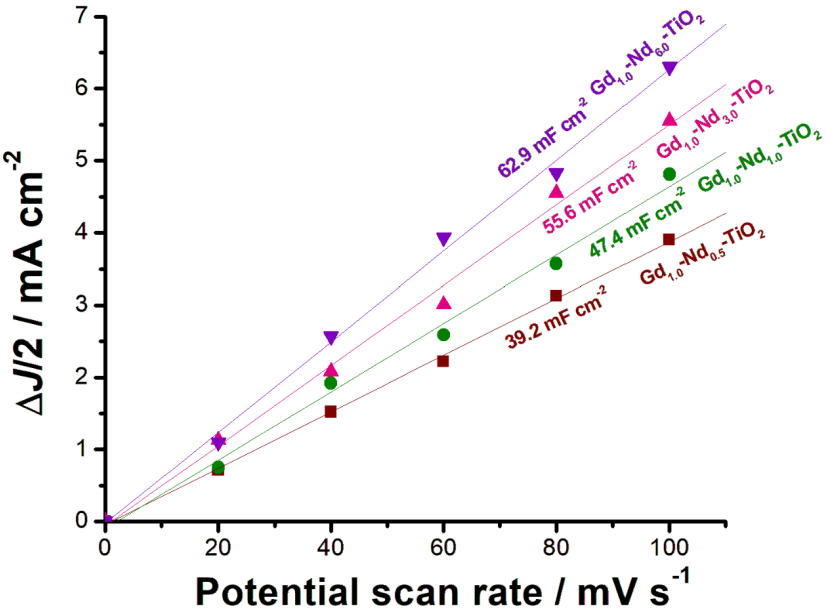

Figure S3. Double-layer capacitance measurements for determining the electrochemically-active surface area of $Gd_{1.0}/Nd_x/TiO_2$ (x = 0.5, 1.0, 3.0, and 6.0 %) catalysts.

Table S1. Comparison of HER catalytic activity of our best performing electrocatalysts with the highly efficient ones reported in the literature in alkaline solutions.

Catalyst	Catalyst loading density / mg cm^{-2}	Tafel slope / mV dec^{-1}	Overpotential @ 10 mA cm^{-2}	Solution	Ref.
$Gd_{1.0}/Nd_{0.5}/TiO_2$	0.28	113	177	1 M KOH	This work
$Gd_{1.0}/Nd_{1.0}/TiO_2$	0.28	112	161	1 M KOH	This work
$Gd_{1.0}/Nd_{3.0}/TiO_2$	0.28	110	142	1 M KOH	This work
$Gd_{1.0}/Nd_{6.0}/TiO_2$	0.28	109	115	1 M KOH	This work
Co-Mo (26 wt.% Mo)	---	---	180	1 M NaOH	[12]
Co-Mo-TiO_2	---	72	68	1 M NaOH	[12]
Co-Mo	---	---	360	1 M KOH	[12]
Co-Mo	---	---	90	8 M NaOH (90°C)	[12]
Co-Mo-C	---	---	200	8 M NaOH (90°C)	[12]
Co-Ni	---	---	550	1 M KOH	[13]
Co-Mo	---	---	145	1 M KOH	[13]
Co-Ni-Mo	---	---	110	1 M KOH	[13]
MoNi hollow structure	---	31.4	38	1 M KOH	[14]
Ni wire		95.8	262	1 M KOH	[15]
Ni-Cu-1.5	---	81.6	180	1 M KOH	[15]
Ni-Cu-3.0	---	57.2	128	1 M KOH	[15]
Ni-Cu-5.4	---	74.5	158	1 M KOH	[15]
NiMo HNRs / Ti mesh	---	---	92	1 M KOH	[16]
NiMo NWs / Ni foam	0.41	---	30	1 M KOH	[16]
NiMo powder	---	---	80	2 M KOH	[16]
Co-P/Ni-P alloys	---	---	100	1 M KOH	[17]
Co-Mo-P amorphous	0.5	63	30	1 M KOH	[17]
Co-Mo-P amorphous	0.5	65	35	1 M KOH	[17]
Co-Mo-P nanocrystal	0.5	---	83	1 M KOH	[17]
Pt-Ni alloy	---	---	82	0.1 M KOH	[18]
$Fe_{75}Mo_{20}Er_5$	---	---	284	Alkaline	[19]
$Fe_{75}Mo_{20}Dy_5$	---	---	262	Alkaline	[19]
$Fe_{75}Mo_{20}Gd_5$	---	---	236	Alkaline	[19]
$Fe_{80}Mo_{20}$	---	---	214	Alkaline	[19]
$Fe_{75}Mo_{20}(MM)_5$	---	103	186	Alkaline	[19]
Fe-Co (1:1) (MW)	---	68	250	Alkaline	[20]
Co	---	134	211	1 M KOH	[21]
CoMoC	3.9	46	46	1 M KOH	[22]
Mo_2C	---	89	146	1 M KOH	[23]

References

1. [1] Head, D.; Mc Carty, G. Acetylation of N-isopropylideneanilines. Formation of a novel 1,3-oxazetidine derivative. Tetrahedron Lett., **1975**, *16*, 1405-1408.

[2] Amine, A.; Imen, B.; Adnen, M.; Noureddine, J.; Leila, S. Hybrid Au-Fe_3O_4 Nanoparticles: Plasmonic, Surface Enhanced Raman Scattering, and Phase Transition Properties. *J. Phys. Chem. C*, **2013**, *117*, 16166-16174.

[3] Ibrahim, M. M.; Mezni, A.; Alsawat, M.; Kumeria, T.; Das, M. R.; Alzahly, S.; Aldalbahi, A.; Gornicka, K.; Ryl, J.; Amin, M. A.; Altalhi, T. Enhanced hydrogen evolution reaction on highly stable titania-supported PdO and Eu_2O_3 nanocomposites in a strong alkaline solution. *Int. J. Energy Res.*, **2019**, *43*, 5367-5383.

[4] Yang, C.; Tang, Y. H.; Lam, W. M.; Lu, W. W.; Gao, P.; Zhao, C. B.; Yuen, M. F. Moisture-cured elastomeric transparent UV and X-ray shielding organic–inorganic hybrids. *J. Mater. Sci.*, **2010**, *45*, 588–3594.

[5] Velasco, M. J.; Rubio, F.; Rubio, J.; Oteo, J. L. Hydrolysis of Titanium Tetrabutoxide. Study by FT-IR Spectroscopy. *Spectrosc. Lett.*, **1999**, *32*, 289–304.

[6] Mezni, A.; Kouki, F.; Romdhane, S.; Fonrose, B.; Joulie, S.; Mlayah, A.; Smiri, L. Facile Synthesis of Cu-doped ZnO Nanoparticle in Triethyleneglycol: Photocatalytic Activities and Aquatic Ecotoxicity. *Mater. Lett.*, **2012**, 86, 153-156
[7] Que, W.; Zhou, Y.; Lam, Y. L.; Chan, Y. C.; Kam, C. H. Sol-gel Preparation and Optical Properties of TiO_2/Organically Modified Silane Hybrid Material Containing DR13. *J. Sol–Gel. Sci. Technol.*, **2001**, *20*, 187–195
[8] Wang, B. L.; Hu, L. L. Polydimethylsiloxane/silica/titania composites prepared by solvent-free sol-gel technique. *Mater. Chem. Phys.*, **2005**, *89*, 417–422.
[9] Vasilyeva, I.; Kuz'micheva, G.; Pochtar, A.; Gainanova, A.; Timaeva, O.; Dorokhov, A.; Podbel'skiy, V. On the nature of the phase "η-TiO_2. *New J. Chem.*, **2016**, *40*, 151-161.
[10] Ibrahim, M. M.; Mezni, A.; El-Sheshtawy, H. S.; Abu Zaid, A. A. ; Alsawat, M.; El-Shafi, N. ; Ahmed, S. I. ; Shaltout, A. A. ; Amin, M. A.; Kumeria, T. ; Altalhi, T. Direct Z-scheme of Cu_2O/TiO_2 enhanced self-cleaning, antibacterial activity, and UV protection of cotton fiber under sunlight. *Appl. Surf. Sci.*, **2019**, *479*, 953-962.
[11] Liu, Y.-R.; Shang, X.; Gao, W.-K.; Dong, B.; Chi, J.-Q.; Li, X.; Yan, K.-L.; Chai, Y.-M.; Liu, Y.-Q.; Liu, C.-G. Ternary CoS_2/MoS_2/RGO Electrocatalyst with CoMoS Phase for Efficient Hydrogen Evolution. *Appl. Surf. Sci.*, **2017**, *412*, 138−145
[12] Wang, C., Bilan, H.K., Podlaha, E.J. Electrodeposited Co-Mo-TiO_2 Electrocatalysts for the Hydrogen Evolution Reaction. *J. Electrochem. Soc.*, **2019**, *166*, F661-F669.
[13] Laszczyńska, A.; Szczygieł, I. Electrocatalytic activity for the hydrogen evolution of the electrodeposited Co–Ni–Mo, Co–Ni and Co–Mo alloy coatings. *Int. J. Hydrogen Energy*, **2020**, *45*, 508-520.
[14] Zhou, Y., Luo, M.; Zhang, W.; Zhang, Z.; Meng, X.; Shen, X.; Liu, H.; Zhou, M.; Zeng, X. Topological Formation of a Mo–Ni-Based Hollow Structure as a Highly Efficient Electrocatalyst for the Hydrogen Evolution Reaction in Alkaline Solutions. *ACS Appl. Mater. Interfaces*, **2019**, *11*, 21998-22004.
[15] Gao, M.Y., et al., Electrochemical fabrication of porous Ni-Cu alloy nanosheets with high catalytic activity for hydrogen evolution. *Electrochim. Acta*, **2016**, *215*, 609-616.
[16] Fang, M., et al., Hierarchical NiMo-based 3D electrocatalysts for highly-efficient hydrogen evolution in alkaline conditions. *Nano Energy*, **2016**, *27*, 247-254.
[17] Thenuwara, A.C., et al., Co-Mo-P Based Electrocatalyst for Superior Reactivity in the Alkaline Hydrogen Evolution Reaction. *ChemCatChem*, **2018**, *10*, 4846-4851.
[18] Zhang, C., et al., The OH−-driven synthesis of Pt–Ni nanocatalysts with atomic segregation for alkaline hydrogen evolution reaction. *J. Mater. Chem. A*, **2019**, *7*, 5475-5481.
[19] Rosalbino, F., et al., Fe-Mo-R (R = rare earth metal) crystalline alloys as a cathode material for hydrogen evolution reaction in alkaline solution. *Int. J. Hydrogen Energy*, **2011**, *36*, 1965-1973.
[20] Cabello, G., et al., Microwave-Electrochemical Deposition of a Fe-Co Alloy with Catalytic Ability in Hydrogen Evolution. *Electrochim. Acta*, **2017**, *235*, 480-487.
[21] Liu, G., et al., A highly efficient alkaline HER Co–Mo bimetallic carbide catalyst with an optimized Mo d-orbital electronic state. *J. Mater. Chem. A*, **2019**, *7*, 12434-12439.